Application and Extension of the Particle X-ray Coincidence Technique (PXCT) to Astrophysical Reaction Rates

L. J. Sun[a], J. Dopfer[b,a], A. Adams[b,a], C. Wrede[b,a,*], A. Banerjee[c], B. A. Brown[b,a], R. Mahajan[a], T. Rauscher[d,e], C. Sumithrarachchi[a], D. Weisshaar[a], T. Wheeler[b,a]

[a]*Facility for Rare Isotope Beams, Michigan State University, East Lansing, Michigan 48824, United States*
[b]*Department of Physics and Astronomy, Michigan State University, East Lansing, Michigan 48824, United States*
[c]*Saha Institute of Nuclear Physics, Kolkata, West Bengal 700064, India*
[d]*Department of Physics, University of Basel, 4056 Basel, Switzerland*
[e]*Centre for Astrophysics Research, University of Hertfordshire, Hatfield AL10 9AB, United Kingdom*

Abstract

Lifetimes of nuclear states are critical for understanding nuclear structure and astrophysical modeling. The Particle X-ray Coincidence Technique (PXCT) was originally developed to measure the average lifetimes in the $10^{-17} - 10^{-15}$ s range for proton-unbound states populated by electron capture (EC). We have designed and built a detection system at the Facilities for Rare Isotope Beams that utilizes and extends PXCT to measure the lifetimes and decay branching ratios of discrete ^{60}Zn resonances populated by ^{60}Ga EC/β^+ decay. The performance of the PXCT system has been thoroughly tested using radioactive sources and is ready for the ^{60}Ga decay experiment in the stopped-beam area of FRIB. This setup will provide essential data to address the competition between the ^{59}Cu$(p, \gamma)^{60}$Zn and ^{59}Cu$(p, \alpha)^{56}$Ni reactions that determines the strength of the NiCu cycle, which is predicted to have significant impacts on the modeling of X-ray burst light curves and the composition of the burst ashes.

1. Introduction

In the 1970s, the Particle X-ray Coincidence Technique (PXCT) was initially demonstrated and applied to measure the average lifetimes of proton-unbound states in ^{69}As as populated by the electron capture (EC) of ^{69}Se [1]. The principle of the method is illustrated in Fig. 1. In the process of an EC-delayed proton emission, a proton-rich precursor with an atomic number of Z decays by K-EC to the proton emitter $(Z-1)$. Due to the EC, a proton unbound nuclear state and an atomic shell vacancy are created simultaneously. An electron in a higher-lying atomic shell fills the vacancy with typical lifetimes of $\tau_{K\text{shell}} = 0.01$ to 1.0 fs and emits the characteristic X ray. Meanwhile, the proton-unbound state with a comparable lifetime $\tau_{p-\text{emit}}$ emits a proton to a state of the daughter $(Z-2)$. If the proton is emitted before the X-ray emission, then the X-ray energy will correspond to the atomic number of the daughter $(Z-2)$. If the proton is emitted after the X-ray emission, then the X-ray energy will be characteristic of the atomic number of the proton emitter $(Z-1)$. By measuring the spectrum of X rays in coincidence with protons and counting the relative intensities of the $(Z-1)$ and $(Z-2)$ X-ray peaks $I_{KX(Z-1)}/I_{KX(Z-2)}$, the lifetimes of proton-emitting states can be related to the lifetimes of the emitter K-shell vacancies by the relation:

$$\frac{\tau_{p-\text{emit}}}{\tau_{K\text{shell}}} = \frac{\Gamma_{K\text{shell}}}{\Gamma_{p-\text{emit}}} = \frac{I_{KX(Z-1)}}{I_{KX(Z-2)}}, \tag{1}$$

where the decay width $\Gamma_{K\text{shell}}$ and $\Gamma_{p-\text{emit}}$ is the equivalent of $\hbar/\tau_{K\text{shell}}$ and $\hbar/\tau_{p-\text{emit}}$, respectively, as they both follow the exponential decay law. Because the K-shell vacancy lifetimes are well known both experimentally and theoretically, ranging from $\tau \approx 2 \times 10^{-15}$ s for carbon down to $\tau \approx 6 \times 10^{-18}$ s for uranium [2, 3], lifetimes of proton-emitting states can be determined by measuring X-ray peak ratios. The preceding discussion is also generalizable to EC-delayed α-particle emission.

So far, the PXCT has been applied in six decay measurements, as summarized in Table 1. In all these cases, only the average sub-fs lifetimes of proton-unbound states populated by EC were obtained. Individual proton-emitting states could not be distinguished due to the high level density. Additionally, the applicability of this technique has not been explored in an astrophysical context. We have built a detection system to extend the PXCT to measure both the lifetimes and branching ratios of individual resonances that are important for modeling explosive astrophysical scenarios. High-resolution measurements on protons and photons would further enhance the PXCT by enabling the selection of the initial proton-emitting states and the excited final states.

---

*Corresponding author
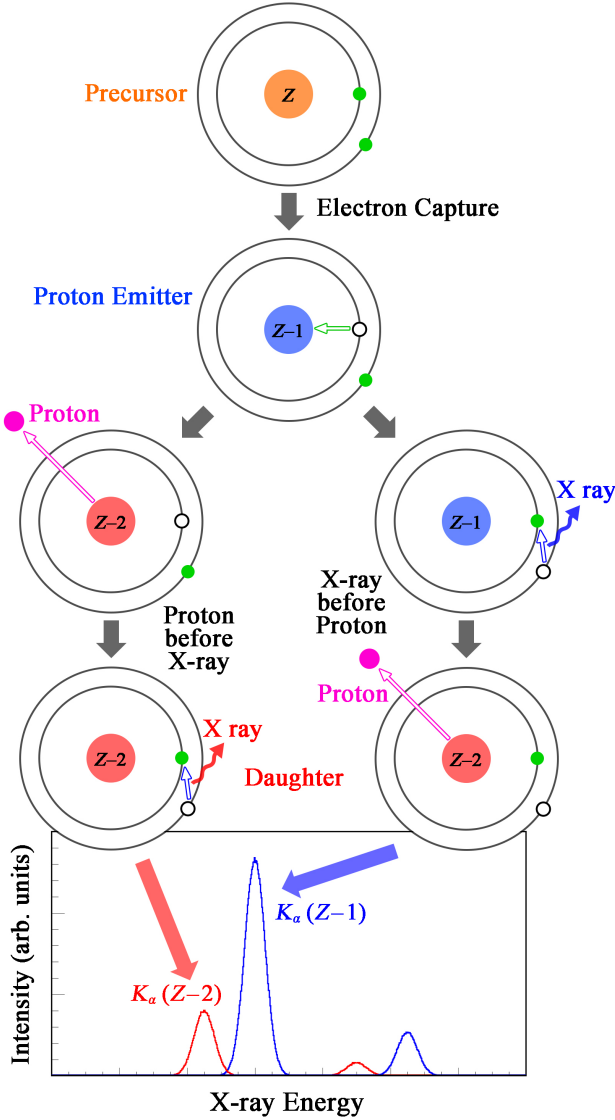Email address:* `wrede@frib.msu.edu` (C. Wrede)

Figure 1: Schematic illustrating the Proton-X-ray Coincidence Technique. See text for details.

Table 1: Properties of all nuclei that have been measured with PXCT. Columns 1–5 list the EC/β^+-decay precursors, the half-lives ($T_{1/2}$), the β-decay energies (Q_{EC}), the proton-separation energies of the EC/β^+-decay daughters (S_p), and the total intensities of EC/β^+-delayed protons (I_p), respectively.

Precursor	$T_{1/2}$ (s)	Q_{EC} (keV)	S_p (keV)	I_p (%)	Literature
^{65}Ge	30.9(5)	6179.3(23)	3942.4(6)	0.011(3)	[4]
^{69}Se	27.4(2)	6680(30)	3420(30)	0.045(10)	[4, 5]
^{73}Kr	27.3(10)	7094(9)	3067(7)	0.25(3)	[4, 6, 7]
^{77}Sr	9.0(2)	7027(8)	3106(4)	0.08(3)	[4]
^{113}Xe	2.74(8)	8916(11)	841(12)	7(4)	[8]
^{117}Ba	1.75(7)	9040(260)	740(60)	16(3)	[9]

2. Astrophysical Motivations

Type I X-ray bursts (XRBs) are the most frequent type of thermonuclear stellar explosions in the Galaxy. They are powered by thermonuclear runaways in hydrogen- and/or helium-rich material accreted onto the surface of a neutron star in a low-mass X-ray binary system. The main nuclear reaction flow in the XRB is driven toward the proton drip-line and to high masses via the triple-α reaction, a sequence of (α, p) and (p, γ) reactions (αp-process), and a series of (p, γ) reactions and β^+-decays (rp-process). Accurate nuclear physics inputs such as β decay rates, masses, and nuclear reaction rates of neutron-deficient rare isotopes along the path of the αp- and the rp-processes are needed to model the energy production and nucleosynthesis in XRBs. Our understanding of XRBs has greatly expanded while they still hold many open questions despite decades of work [10, 11, 12].

As indicated in Fig. 2, under XRB conditions, the rp-process beyond ^{56}Ni may be affected by several cycles. A low ^{59}Cu(p, γ)^{60}Zn rate or a high ^{59}Cu(p, α)^{56}Ni rate leads to the formation of a stronger NiCu cycle that returns the reaction flux to ^{56}Ni, which would strongly impede the synthesis of heavier nuclei and also affects the XRB observables [13]. The critical quantity determining the strength of the NiCu cycle is the ratio of the (p, α) to (p, γ) reaction rates at ^{59}Cu. Currently, both rates recommended by REACLIB [14] are calculated by the Hauser-Feshbach statistical model [15]. The variations in these rates have been identified as having a significant impact on the modeling of XRB light curves and the composition of the burst ashes [16, 17, 18]. The competition between ^{59}Cu(p, γ)^{60}Zn and ^{59}Cu(p, α)^{56}Ni reactions at higher temperatures (~ 3 GK) is found to have a significant impact on the νp process nucleosynthesis in core-collapse supernovae [19, 20]

For ^{59}Cu + p resonant capture through narrow resonances, the resonant capture reaction rate can be calculated using the well-known relation [21],

$$N_A \langle \sigma v \rangle_r = 1.5394 \times 10^{11} (\mu T_9)^{-3/2} \times \omega \gamma$$
$$\times \exp\left(-\frac{11.605 E_r}{T_9}\right) (\text{cm}^3 \text{s}^{-1} \text{mol}^{-1}), \quad (2)$$

where $\mu = A_p A_T / (A_p + A_T)$ is the reduced mass in atomic mass units, with $A_p = 1$ and $A_T = 59$ as the mass numbers of proton and ^{59}Cu, respectively. E_r is the resonance energy in the center-of-mass system in units of MeV. T_9 is the temperature in units of giga kelvin (GK), and $\omega \gamma$ is the resonance strength in units of MeV. For the ^{59}Cu(p, γ)^{60}Zn resonance:

$$\omega \gamma = \frac{2J_r + 1}{(2J_p + 1)(2J_T + 1)} \frac{\Gamma_p \Gamma_\gamma}{\Gamma_{tot}}, \quad (3)$$

where J_r is the spin of the resonance, $J_p = 1/2$ is the spin of proton, and $J_T = 3/2^-$ is the spin of the ground state of ^{59}Cu. The total decay width Γ_{tot} of the resonance is the sum of the partial decay widths, which include proton width (Γ_p), γ width (Γ_γ), and α width (Γ_α) for the resonances relevant to XRBs. Equivalently, the resonance strength can be constructed
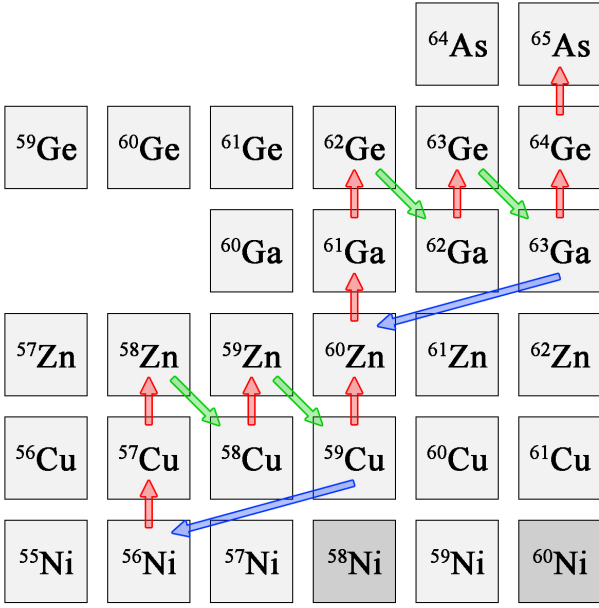
Figure 2: Portion of the *rp*-process reaction sequence featuring the NiCu cycle and ZnGa cycle. ^{58}Ni and ^{60}Ni are stable.

by combining the proton branching ratio $B_p = \Gamma_p/\Gamma_{\text{tot}}$, the γ-ray branching ratio $B_\gamma = \Gamma_\gamma/\Gamma_{\text{tot}}$, and the lifetime τ using the following expression:

$$\omega\gamma = \frac{2J_r + 1}{(2J_p + 1)(2J_T + 1)} B_p B_\gamma \frac{\hbar}{\tau}, \tag{4}$$

where $\hbar$ is the reduced Planck constant. This relation is also applicable to the ^{59}Cu$(p, \alpha)^{56}$Ni resonance by replacing the γ terms with α terms ($J_\alpha = 0$). Therefore, measurements of the proton, γ-ray, and α-decay branching ratios, and the lifetimes of the ^{60}Zn resonances within the Gamow window will suffice to determine the contribution of resonant capture. Instead of using separate measurements for branching ratios and lifetimes, applying the PXCT on ^{60}Ga EC offers the unique advantage of obtaining both quantities in one experiment.

In a recent ^{58}Ni$(^3$He$, n)^{60}$Zn reaction measurement [22], the nuclear level density of ^{60}Zn was extracted from the neutron evaporation spectrum. At $E_x = 6$ MeV, the level density is estimated to be only ~18 MeV^{-1}. Table 2 summarizes the spins and parities of relevant ^{60}Zn resonances. It is evident that the negative parity states associated with $\ell = 0, 2$ proton captures are not accessible via allowed β transitions, also indicating that we will deal with an even lower level density in the β decay study.

Even if the level density selected by β decay is still too high to distinguish discrete resonances, we can derive the particle and γ-transmission coefficients and the level density of excited states, which are essential ingredients to calculate the reaction rates within the statistical model [15]. The standard approach when using a Hauser-Feshbach statistical model is to include a number of discrete excited states when experimentally known [23]. A direct measurement of the ^{59}Cu$(p, \alpha)^{56}$Ni

Table 2: Properties of ^{60}Zn states populated via proton captures on the $3/2^-$ ^{59}Cu ground state and the $1/2^-$ ^{59}Cu first excited state, and the allowed β transitions of the 2^+ ^{60}Ga ground state.

Population	^{60}Zn states
$\ell = 0$ p on $3/2^-$	$1^-, 2^-$
$\ell = 1$ p on $3/2^-$	$0^+, 1^+, 2^+, 3^+$
$\ell = 2$ p on $3/2^-$	$0^-, 1^-, 2^-, 3^-, 4^-$
$\ell = 0$ p on $1/2^-$	$0^-, 1^-$
$\ell = 1$ p on $1/2^-$	$0^+, 1^+, 2^+$
$\ell = 2$ p on $1/2^-$	$1^-, 2^-, 3^-$
β decay from 2^+	$1^+, 2^+, 3^+$

reaction using a reaccelerated ^{59}Cu beam and a cryogenic solid H$_2$ target at center-of-mass energy $E_{\text{c.m.}} = 6.0$ MeV found that ^{59}Cu(p, α) proceeds predominantly to ^{56}Ni ground state, and standard statistical model calculations overestimate the cross section by a factor of 1.6−4 [24]. The nuclear level density in the compound nucleus ^{60}Zn may not be sufficiently high to justify a statistical treatment. Kim *et al.* [25] evaluated available experimental data on ^{60}Zn resonances, supplemented with theoretical calculations. They found the ^{59}Cu$(p, \alpha)^{56}$Ni reaction rate to be lower than the REACLIB rate [14] at XRB temperatures, indicating a weaker NiCu cycle strength than previously estimated. There are other ongoing efforts to obtain ^{60}Zn nuclear structure information, such as populating ^{60}Zn states via the ^{59}Cu$(d, n)^{60}$Zn transfer reaction [26], and ^{60}Ga total absorption spectroscopy [27]. However, experimental constraints on the ^{59}Cu$(p, \gamma)^{60}$Zn and ^{59}Cu$(p, \alpha)^{56}$Ni are still scarce and limit a robust understanding of their astrophysical impacts.

3. ^{60}Ga Data Evaluation

Fig. 3 summarizes currently known ^{60}Ga decay properties. The mass excesses and particle separation energies of ^{56}Ni, ^{59}Cu, and ^{60}Zn reported by AME2020 [28] are all of sub-keV precision, while the mass of ^{60}Ga is only estimated to be $-39590(200)$ keV. A recent ^{60}Ge β-decay study measured the energies of protons and γ rays emitted from the $T = 2$ isobaric analog state in ^{60}Ga. Combining with the known mass of ^{59}Zn [28], the mass excess of ^{60}Ga is determined to be $-40016(15)$ keV, where the dominant uncertainty is from their measured proton energies [29]. At the Ion Trap for Atomic and Nuclear Science of TRIUMF, a direct mass measurement using the multiple-reflection time-of-flight mass spectrometer reported a consistent ^{60}Ga mass value of $-40005(30)$ keV [30]. We obtain the mass of ^{60}Ga to be $-40014(15)$ keV by taking a weighted average of Refs. [29, 30]. The corresponding proton-separation energy and the β-decay Q-value of ^{60}Ga are obtained to be $S_p = 87(15)$ keV and $Q_{\text{EC}} = 14161(15)$ keV, respectively.

The Gamow energies and windows for the ^{59}Cu$(p, \gamma)^{60}$Zn and ^{59}Cu$(p, \alpha)^{56}$Ni reactions shown in Table 3 are calculated from a numerical study of the relevant energy ranges for
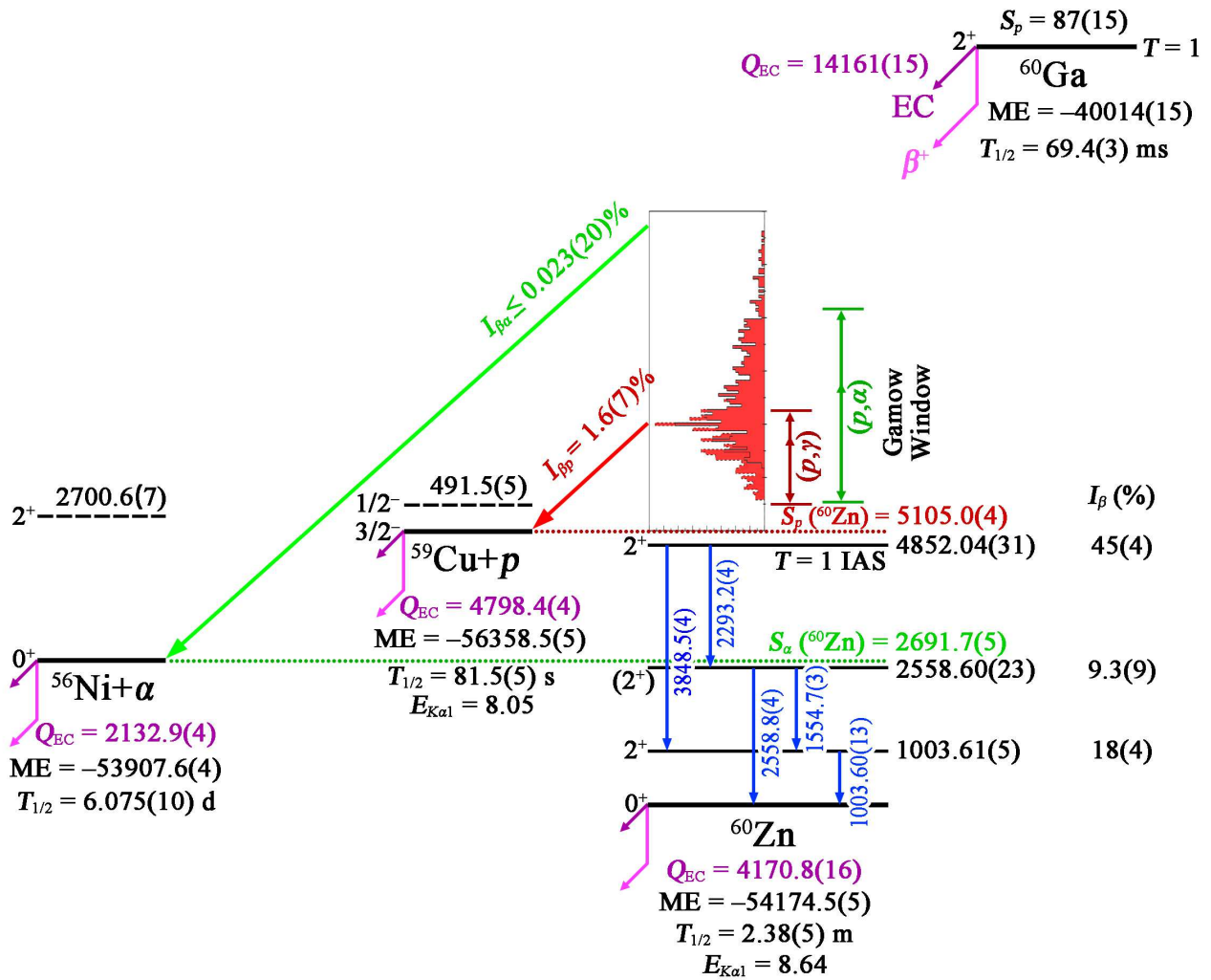
Figure 3: Known decay scheme of ^{60}Ga. All energies labeled in the scheme are given in units of keV. The proton spectrum is extracted from only available βp measurement [35]. The two dashed lines indicate the first excited states of ^{56}Ni and ^{59}Cu, respectively, which have not been observed in ^{60}Ga decay. The two double-headed arrows indicate the Gamow windows for the ^{59}Cu$(p, \gamma)^{60}$Zn and ^{59}Cu$(p, \alpha)^{56}$Ni reactions, respectively, according to the calculation in Table 3. See text for other data evaluation.

astrophysical reaction rates [31]. It can be seen that at any given temperature below 3 GK, the corresponding effective energy windows will not exceed 4.2 MeV. Combined with the proton-separation energy of ^{60}Zn $S_p(^{60}$Zn$) = 5105.0(4)$ keV and α-separation energy of ^{60}Zn $S_\alpha(^{60}$Zn$) = 2691.7(5)$ keV, the ^{60}Zn resonances of interest range from 5.6 to 9.3 MeV, which are energetically accessible in the β decay of ^{60}Ga owing to the large $Q_{EC}(^{60}$Ga$) = 14161(15)$ keV.

The half-lives of ^{56}Ni [32], ^{59}Cu [33], and ^{60}Zn [34] are all well-determined. The half-life of ^{60}Ga has been measured to be $T_{1/2} = 70(15)$ ms [35], 70(13) ms [36], 76(3) ms [37], and 69.4(2) ms [29], and we obtain the weighted average to be 69.4(3) ms.

^{60}Ga is observed to decay by βp with an intensity of $I_p = 1.6(7)\%$ and possibly by $\beta\alpha$ with $I_\alpha \leq 0.023(20)\%$ [35]. ^{56}Ni, ^{59}Cu, and ^{60}Zn decay via low-energy $\beta\gamma$ only. Mazzocchi *et al*. [35] reported 5 ^{60}Ga$(\beta\gamma)$ through 3 proton-bound states in ^{60}Zn. Orrigo *et al.*. [29] confirmed these $\beta\gamma$ and proton-bound states and reported 24 new $\beta\gamma$ that are correlated with ^{60}Ga implants. However, they did not place any of these new transitions in the decay scheme, and it is possible that some of them may be escape peaks. Orrigo *et al.*. did not report any β-feeding intensities, so we deduce the β-feeding intensities based on the γ intensities reported by [29]. Fig. 3 lists the weighted average of β-feeding intensities [29, 35]. It should be noted that approximately 26% β-feeding intensities remain unaccounted for. No ^{56}Ni or ^{59}Cu γ rays have been observed in either of ^{60}Ga β-decay spectroscopy [29, 35]. Fig. 3 includes the 5 confirmed ^{60}Zn γ-ray energies by taking the weighted average of all available measurements [29, 35, 38, 39]. We incorporate these newly evaluated γ-ray energies into the $A = 60$ evaluation [34] and perform a least-squares fit to γ-ray energies to obtain adjusted excitation energies [40]. All the spins and parities are adopted from the previous evaluations [32, 33, 34], with the 4852-keV state in ^{60}Zn changed from (2$^+$) to 2$^+$ based on the unambiguous $T = 1$ isobaric analog state argument [29, 35].

To narrow down the important resonances populated in the β-decay of ^{60}Ga, we performed shell-model calculations in the full fp-shell model space with the GPFX1A Hamiltonian [41] using the NuShellX@MSU code [42]. We obtained the spectroscopic factors and partial widths of 67 positive parity ^{60}Zn states within excitation energies of $5.1 - 6.5$ MeV and calculated the resonant capture ^{59}Cu$(p, \gamma)^{60}$Zn reaction rate. As shown in Table 4, the resonant capture contributions from four resonances are found to dominate the total rate over a certain temperature range. A quenching factor $q^2 = 0.6$ for the matrix elements of the Gamow-Teller operator was used to calculate the β-feeding intensities in the ^{60}Ga decay. If certain key resonances can be constrained, we may be able to establish a lower limit for the ^{59}Cu$(p, \gamma)^{60}$Zn reaction rate. A strong lower limit on the ^{59}Cu$(p, \gamma)^{60}$Zn rate would indicate very weak NiCu cycling and potentially solve the astrophysical problem.

Table 3: Gamow windows $\widetilde{E}_{hi} - \widetilde{\Delta} \le E \le \widetilde{E}_{hi}$ and Gamow peaks $\widetilde{E}_0$ for the ^{59}Cu$(p, \gamma)^{60}$Zn and ^{59}Cu$(p, \alpha)^{56}$Ni reactions at a temperature T.

	^{59}Cu$(p, \gamma)^{60}$Zn			^{59}Cu$(p, \alpha)^{56}$Ni		
T (GK)	$\bar{E}_{hi} - \widetilde{\Delta}$ (MeV)	$\bar{E}_0$ (MeV)	$\bar{E}_{hi}$ (MeV)	$\bar{E}_{hi} - \widetilde{\Delta}$ (MeV)	$\bar{E}_0$ (MeV)	$\bar{E}_{hi}$ (MeV)
0.5	0.51	0.71	0.92	0.55	0.74	0.98
1.0	0.67	0.91	1.26	0.73	1.01	1.48
1.5	0.75	1.01	1.57	0.87	1.27	2.11
2.0	0.82	1.14	1.83	1.01	1.74	2.80
2.5	0.85	1.40	2.05	1.24	2.19	3.52
3.0	0.89	1.49	2.26	1.51	2.66	4.16

Table 4: Properties of the dominant resonances in the ^{59}Cu$(p, \gamma)^{60}$Zn reaction predicted by shell model. The values listed in the first through seventh columns are the dominating region of temperature, spin and parity (J^π), excitation energy (E^*), resonance energy (E_r), log ft values, β-feeding intensity (I_β) and ratio of EC/β+ feedings [43] of each resonance, respectively.

T (GK)	J^π	E^* (keV)	E_r (keV)	log ft	$I_{\beta+}$ (%)	$R_{EC/\beta+}$
0.10 − 0.15	3^+	5362	257	6.668	0.03	0.0015
0.15 − 0.45	1^+	5568	463	4.707	2.53	0.0016
0.45 − 0.70	2^+	5648	543	6.091	0.10	0.0017
0.70 − 7.50	2^+	6079	974	5.505	0.29	0.0020

4. Experimental Setup

4.1. Beam delivery

The Facility for Rare Isotope Beams (FRIB) full-power linear accelerator [44] will accelerate ^{70}Ge or ^{78}Kr to 256 MeV/u with a beam power up to 400 kW. The reaction products from ^{70}Ge or ^{78}Kr impinging on a rotating carbon target will be separated by the Advanced Rare Isotope Separator [45]. A cocktail fast beam containing ^{60}Ga and some nearby isotones will be slowed down in metal degraders with momentum compression and thermalized in gas stoppers filled with helium [46, 47]. The thermalized ^{60}Ga ions will drift towards a nozzle and exit into a radio-frequency quadrupole ion-guide system. The ions will be guided and accelerated to 30 keV through a combination of radio-frequency and direct-current fields before being delivered to the stopped beam area [48]. The intensity of the ^{60}Ga stopped beam is estimated to be up to 9×10^3 pps.

As shown in Fig. 4, we have designed and built a PXCT detection system that will be used in the stopped beam area. The beam will be tuned into our vacuum chamber and implanted into an aluminized Mylar foil tilted at a 45° angle with respect to the beam direction. Thermalized beams can be fully stopped by a thin collection foil, thereby reducing the attenuation of photons and charged particles as compared to using fast beams. The detection system comprises a silicon detector telescope for charged-particle detection via energy-loss and residual energy (ΔE-E), a planar germanium detector for X-ray detection, and two large-volume coaxial germanium detectors for γ-ray detection. A Faraday cup will be placed at the target position during the beam tuning. The detection setup can provide characteristic charged particles and γ rays from decay that will aid online beam identification.

4.2. Detectors

We selected two single-sided single-area circular Si detectors, MSD12 of 12 μm thickness [49] and MSD26 of 1000 μm thickness [50] manufactured by Micron Semiconductor Ltd to construct the ΔE-E telescope. The numbers following "MSD" indicate the active area diameter in millimeters. The dead layer window and metallization type for MSD12 are 9.5P/7P, and for MSD26 are 9.5P/2M. Here, 9.5 represents a boron-doped silicon dead layer with a thickness of 50 nm, 7 represents a dead layer with a thickness of 300 nm, and 2 represents a dead layer with a thickness of 500 nm. "P" denotes a periphery metal band with a width of 30 μm around the edge of the active areas and contact pads for wire bonding. The majority of the active area does not have metal coverage. "M" denotes a continuous aluminum coverage with a thickness of 300 nm over the entire active area region. Both silicon chips are assembled onto an FR4-printed circuit board. MSD26 is positioned 15.7 mm from the target center and covers 11.5% of the 4π solid angle. MSD12 is 11.2 mm from the target center and defines the solid angle coverage of the ΔE-E telescope at 5.9% of 4π.

We selected a Low Energy Germanium detector (LEGe), Mirion GL0510, for X-ray detection [51]. The LEGe detector consists of a Ge crystal with a diameter of 25.0 mm and a length of 10.5 mm. LEGe is housed in a flanged-style cryostat with a diameter of 38.1 mm and a 0.13-mm thick beryllium entrance window. The endcap is inserted into the vacuum chamber with its entrance window only 11.0 mm from the target center. The Ge crystal is positioned 5.6 mm from the entrance window, subtending 10.1% of the 4π solid angle. LEGe is fabricated with a thin p^+ contact on the front and side and a rear n^+ contact that covers less than the full area, resulting in lower capacitance than a similar-sized planar device. Since preamplifier noise is a function of detector capacitance, the low capacitance feature makes LEGe ideally suited for X-ray spectroscopy down to 3 keV.

We selected two Extended Range Coaxial Germanium Detectors (XtRa), Mirion GX10020, for γ-ray detection [52]. The active volume of XtRa1 has a diameter of 84.8 mm and a thickness of 65.2 mm, while XtRa2 has a diameter of 79.8 mm and a thickness of 80.0 mm. The Ge crystals are positioned 6.8
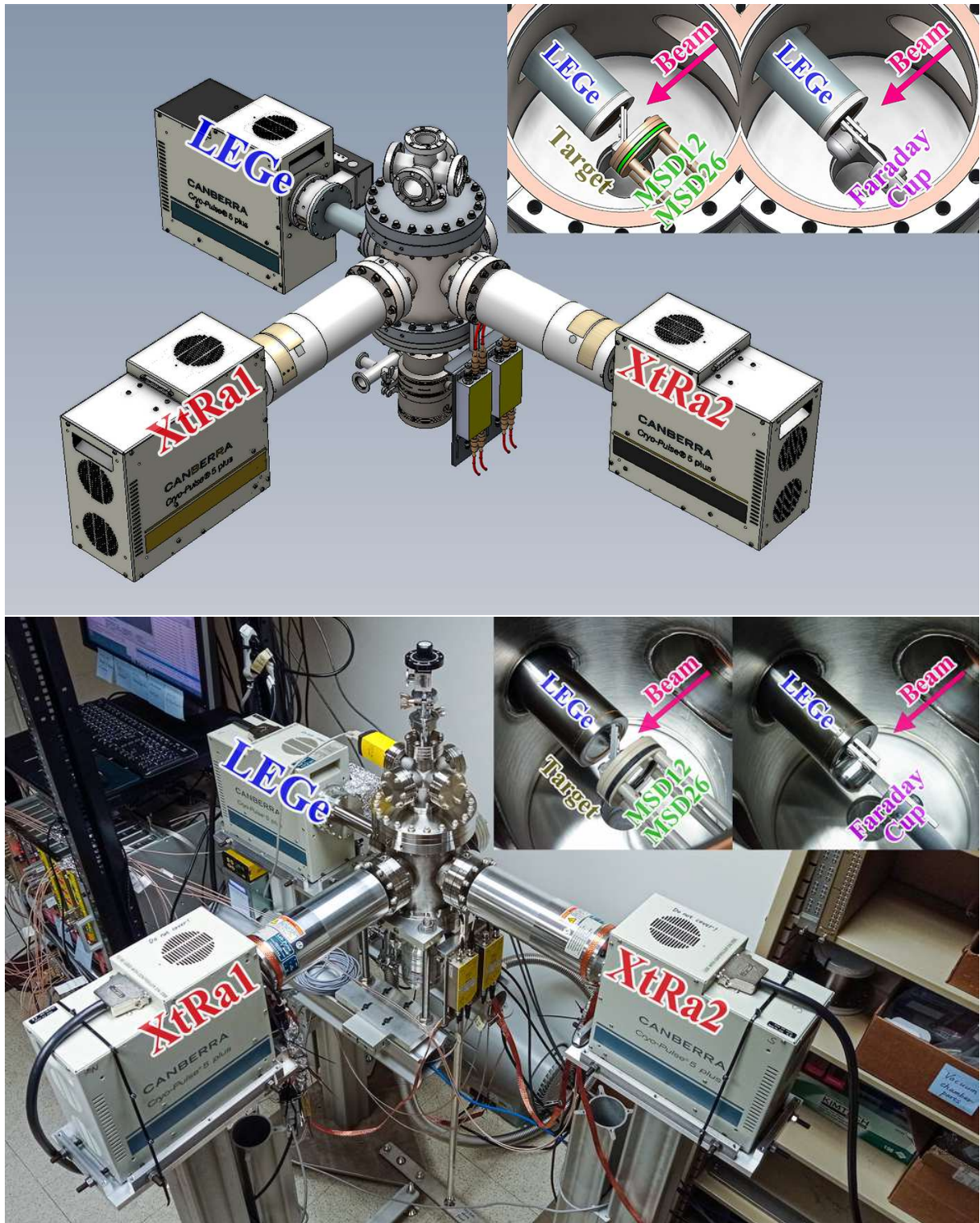
Figure 4: Mechanical design drawing and photograph of the PXCT detection system. The insets highlight two configurations for the detectors inside the central chamber: a Faraday cup with a collimator for beam tuning or a target foil and Si detectors for decay measurements.

and 6.3 mm, respectively, from the entrance windows. Conventional coaxial detectors have a lithium-diffused n^+ contact typically of 0.5 to 1.5 mm thickness on the outer surface, which forms a dead layer that stops most photons below 40 keV, rendering the detector inefficient at low energies. However, the XtRa detectors feature an exclusive thin window contact on the front surface and a n^+ contact on the side. The cryostat window is made of a 0.6-mm-thick carbon composite, enabling a good low-energy response.

All three Ge detectors are equipped with the Cryo-Pulse 5 Plus (CP5-Plus) electrically refrigerated cryostat [53]. A 5-watt pulse tube cooler is integrated into a compact coldhead assembly, which is directly attached to the detector housing. The assembly is connected to a bench-top power controller that provides the required output voltage to drive the compressor. The controller also contains the necessary logic to ensure the safe and reliable operation of the cryostat. An RS-232 serial interface and CP5-Plus control panel application are also included, allowing for remote monitoring of the cooler status. The CP5-Plus is estimated to have a Mean Time To Failure of 3 million hours [54].

4.3. Electronics

The Ge is connected to the Intelligent Preamplifier (iPA) [55], which incorporates a low-noise field-effect transistor (FET) input circuit optimized for the ultra-high source impedance of germanium detectors. The input circuits are cooled by mounting them inside the cryostat. The first stage of iPA serves as an integrator, providing an output voltage proportional to the accumulated charge from the detector, and also functions as an electrometer for measuring the leakage current of the detector. The second stage acts as an output buffer and allows for four conversion factors of 50, 100, 250, and 500 mV/MeV. The iPA generates an inverted output signal that is split into two outputs, each with a termination impedance of 93 and 50 Ω. A USB interface and a control panel application provide real-time monitoring of detector current, temperatures, and preamplifier operating voltages. The four output gains, as well as external or internal test pulsers, are selectable via the control panel application. iPA is equipped with a warm-up sensor that is thermally connected to the detector. The coldhead is also equipped with temperature sensors. In the event that the temperature exceeds the normal operating range, these sensors trigger the high-voltage inhibit signal from the preamplifier and the controller, respectively, providing protection to the Ge detectors.

Two ORTEC 660 Dual Bias Supply modules [56] are used to provide bias voltages to the three Ge detectors. We apply a negative bias to the p^+ contacts of LEGe and a positive bias to the n^+ contacts of XtRa. LEGe becomes fully depleted at -600 V and is recommended to be operated at -1100 V. XtRa1 and XtRa2 become fully depleted at a bias voltage of $+4000$ V and $+2200$ V, respectively, and both operate at $+4500$ V. ORTEC 660 includes a remote bias shutdown feature to protect the preamplifier FET against damage in the instance of accidental warm-up of the Ge detector. The typical leakage currents of the two XtRa detectors are below 20 pA and below 100 pA for LEGe. A Mesytec MHV 4-channel bias supply module with remote control features provides the bias voltages to the two MSD Si detectors. MSD12 has a depletion voltage of 1.5 V and is operated at 3.0 V, and MSD26 has a 90-V depletion voltage and is operated at 130 V. We apply a negative bias to the p^+ contacts of both MSD detectors through MPR-1 charge-sensitive preamplifiers [57] and the n^+ contacts are grounded. MHV offers a ramp speed as low as 5 V/s to protect the circuits of preamplifiers [58]. MSD26 has a leakage current of approximately 60 nA, whereas MSD12 maintains a leakage current below 1 nA. All the preamplifiers are powered by two Mesytec MNV-4 NIM power distribution and control modules [59].

4.4. Data acquisition

All the preamplifier signals are transmitted via double-shielded RG316 coaxial cables of equal length and then digitized by a 16-bit, 250 MHz Pixie-16 module manufactured by XIA LLC [60]. The input impedance of each channel in Pixie-16 is configured to be 1 kΩ. A general-purpose nuclear physics data acquisition system Digital Data Acquisition System (DDAS) is used [61, 62] for recording and processing data. Trapezoidal filtering algorithms are implemented in both the slow filter for pulse amplitude measurement and the fast filter for leading-edge triggering. Each event is timestamped using a Constant Fraction Discriminator (CFD) algorithm based on the trigger filter response. The system operates in an internally triggered mode: recording data on a channel-by-channel basis whenever the trigger filter crosses the user-defined threshold. The data from all channels is ordered in time and subsequently assembled into events based on a user-defined event window length. The event timestamp is counted with 125 MHz clock ticks, i.e., 8 ns intervals.

The tail pulses from MPR-1 exhibit rise times of 400 ns (MSD12) and 70 ns (MSD26), with a 120 μs decay constant. The tail pulses from iPA exhibit rise times of 150 ns (LEGe) and 250 ns (XtRa), with a 50 μs decay constant. The DDAS filter parameters are optimized based on these observations [62, 63, 64]. The pulse amplitude is extracted from the energy filter amplitude at approximately rise time + gap time after triggering. If a second trigger arrives within rise time + gap time, a pileup will occur. The energy filter parameters are the dominant factor in determining the count rate capacity of the DDAS system. A DB-2 Random Pulser [65] is used to investigate the data acquisition dead time. The time intervals between successive pulses obey a Poisson distribution function. The count rate performance is shown in Fig. 5. The observed event losses are in line with pile-up rates defined by the energy filter settings [61].
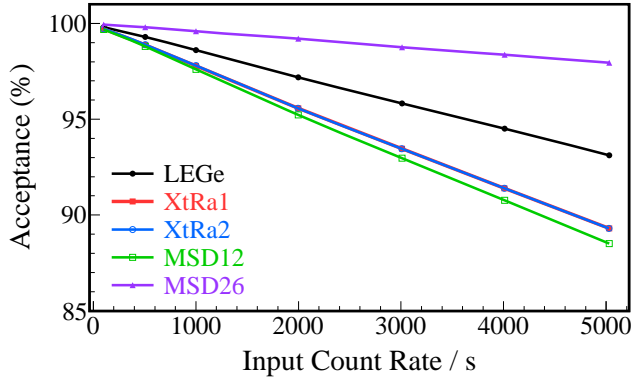
8

Figure 5: DDAS count rate performance.

5. Performance Tests

We have performed comprehensive tests on the PXCT system using the electronics configuration illustrated in Fig. 6.
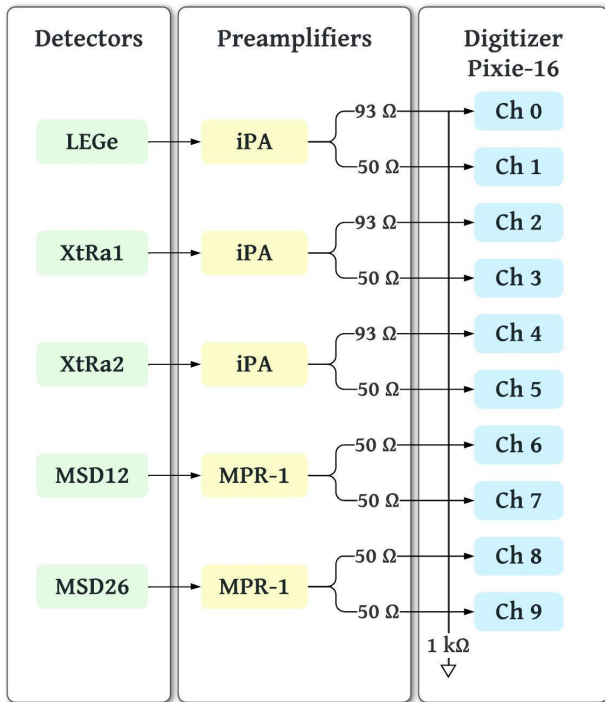

Figure 6: Schematic diagram of the electronics setup. The two arrows following each preamplifier indicate dual outputs with their respective impedance.

5.1. X-ray measurements

We have evaluated the performance of LEGe using the X rays and low-energy γ rays from ^{55}Fe, ^{152}Eu, and ^{241}Am radioactive sources, as shown in Fig. 7. The overall energy resolution achieved by LEGe is characterized by fitting the well-known X-ray or γ-ray lines with an exponentially modified Gaussian (EMG) function to account for incomplete

charge collection [66, 67] at 5.90 keV (Mn $K_{\alpha 1}$), 6.49 keV (Mn $K_{\beta 1}$), 11.89 keV (Np L_{ℓ}), 13.76 keV (Np $L_{\alpha 2}$), 13.95 keV (Np $L_{\alpha 1}$), 26.34 keV (^{237}Np γ), 33.20 keV (^{237}Np γ), 39.52 keV (Sm $K_{\alpha 2}$), 40.12 keV (Sm $K_{\alpha 1}$), 45.29 keV (Sm $K_{\beta 3}$), 45.41 keV (Sm $K_{\beta 1}$), and 59.54 keV (^{237}Np γ). At the energies of interest, 8.05 keV (Cu $K_{\alpha 1}$) and 8.64 keV (Zn $K_{\alpha 1}$), the full width at half maximum is estimated to be 238(8) and 241(7) eV, respectively, providing enough resolving power to distinguish between the characteristic X rays of the proton emitter Zn and the daughter Cu.

For photons below 100 keV interacting with Ge, the photoelectric effect is predominant, i.e., the photon is absorbed, and its energy is transferred to an electron and causes prompt emission of a characteristic X ray as the resulting vacancy in the electron shell is filled. A full-energy peak is still observed if this X ray is reabsorbed near the original interaction site. However, if the photoelectric interaction occurs near the surface of Ge, the X ray is more likely to escape, which results in peaks usually at 9.89 keV and 10.98 keV below the photopeaks, known as the Ge escape peaks (Fig. 7). These energy differences correspond to the characteristic $K_{\alpha 1}$ and $K_{\beta 1}$ X-ray energies for Ge, respectively [68].

For photon energies just above the K-shell binding energy of Ge, 11.1030(20) keV [68], the incident photon is strongly absorbed without deep penetration beyond the detector surface. The subsequent characteristic K X ray tends to escape, thereby decreasing the full energy peak efficiency. This phenomenon can potentially complicate the normalization of near-edge X rays. However, for our energies of interest in the range of 8-9 keV, K-shell absorption is no longer possible, and L-shell interactions dominate. In this case, incident gamma rays tend to penetrate somewhat deeper, and the energy of the fluorescent Ge L X rays is just $1.0-1.4$ keV, resulting in a reduced probability of escape. By integrating the L X rays within the energy range of $5.4-8.1$ keV in the ^{152}Eu spectrum in Fig. 7 and comparing it with the X-ray emission intensities [69], we estimate the corresponding detection efficiency to be 4.02(13)%, in which only statistical uncertainties are considered.

5.2. γ-ray measurements

Figure 8 shows the γ-ray spectra measured by XtRa1 and XtRa2 using an ^{152}Eu point source. The achieved energy resolution aligns with the specifications provided by the manufacturer. Both XtRa detectors record an average of 300 room background gamma rays per second in our lab test environment. We first placed the source at the midpoint between the two XtRa detectors that were facing each other, with a distance of 28 cm between them. We then placed the source at the center of the vacuum chamber. The two XtRa detectors were placed as close as possible to the two flanges (Fig. 4), with their entrance windows about 12 mm from the flange surface. XtRa1 Ge crystal has a slightly larger diameter than XtRa2. Both Ge crystals are 158.5 mm from the target center, covering 1.70% and 1.51% of the 4π solid angle, respectively. As can be seen from Fig. 8, both XtRa detectors
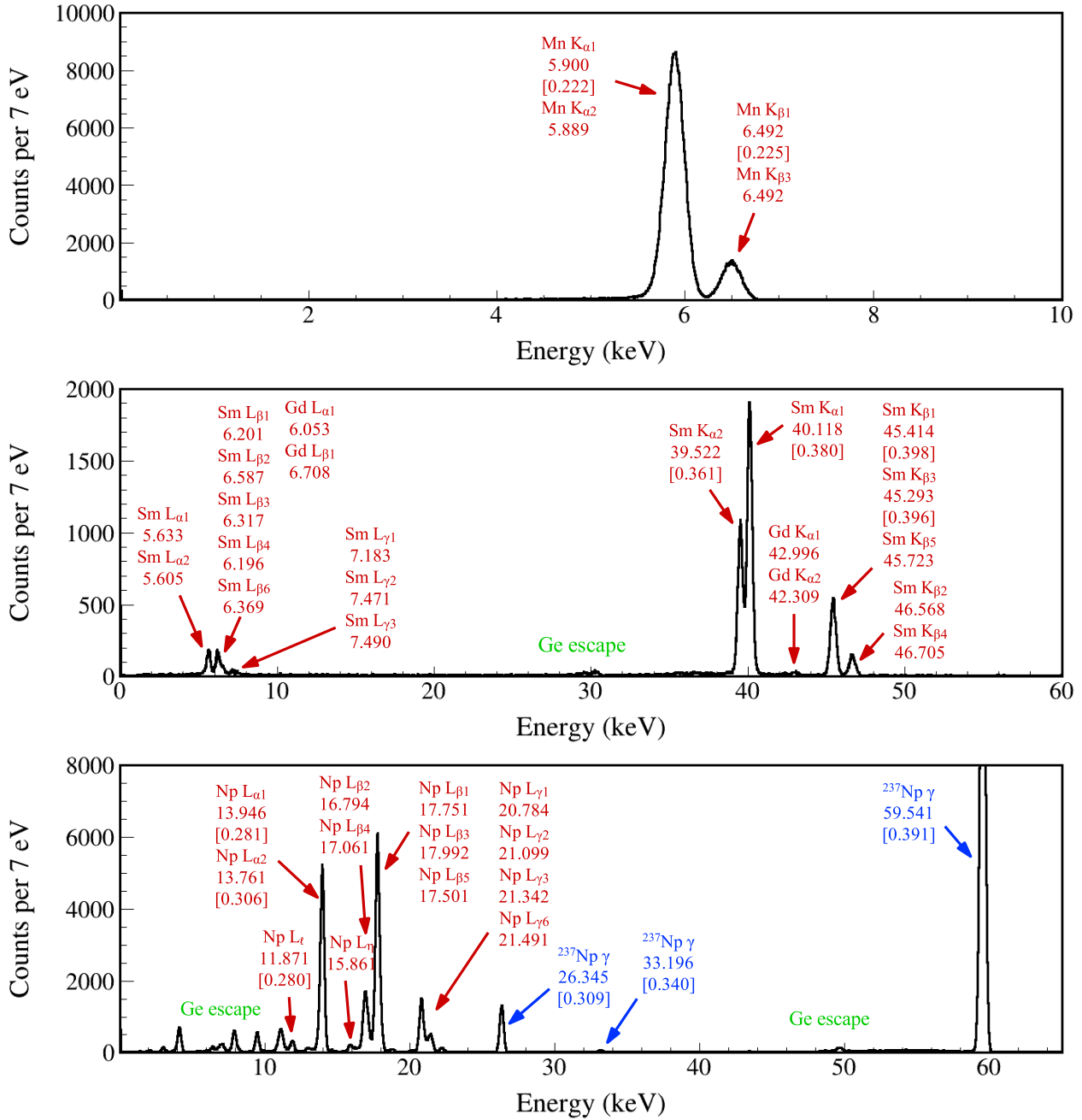
Figure 7: X-ray and/or γ-ray spectra measured by the LEGe detector using [55]Fe (top), [152]Eu (middle), and [241]Am (bottom) sources. All the X-ray energy values are adopted from Ref. [68] rounded to the nearest 0.01 keV. All the γ-ray energy values are adopted from Ref. [70] rounded to the nearest 0.01 keV. The FWHM values used to characterize the energy resolution of LEGe are indicated within brackets.

exhibit good low-energy response to the ^{152}Eu X rays at 40 keV, while when the source is placed inside the chamber, the X rays are effectively blocked by the 3.175-mm thick stainless steel flanges.

We also tested XtRa detectors with ^{60}Co and ^{137}Cs sources placed at the center of the chamber. The activity of the ^{152}Eu calibration source is quoted with 1.4% accuracy by the manufacturer [72]. The activities of the ^{60}Co and ^{137}Cs sources both have a 3% uncertainty. MSD12 was not in place during these tests due to its fragility. MSD26 and the Si detector holders attenuated the γ rays from the source to XtRa2 but had little effect on XtRa1. XtRa1 and XtRa2 have an absolute full-energy peak efficiency of 0.334(3)% and 0.286(3)% at 1 MeV, respectively, based on an exponential function that contains a polynomial of degree i with the natural logarithm of the energy E: $\varepsilon(E) = \exp\left[\sum_{i=0}^{6} p_i \ln(E)^i\right]$ fit on all the data points [73]. The error bars on the data points reflect the uncertainty of the γ-ray yields and the source activities, with an additional 2.5% to account for the true coincidence summing effect. We have developed a detailed Monte Carlo simulation using GEANT4 [74, 75] to extend the γ-ray detection efficiency curve to high energies (Fig. 9). The simulation takes into account the geometry of the setup and the detector response characterized by fitting the measured γ-ray lineshapes with the EMG function. Monoenergetic γ rays were emitted isotropically according to the source distribution and interacted with the surrounding materials. The photopeak efficiency was extracted from the output spectrum. We then fit the ratio of the simulated efficiency to the measured efficiency between 0.5-1.5 MeV and obtained constant ratios of 1.143(10) and 1.195(10) for XtRa1 and XtRa2, respectively, which serve as the normalization factors to match the simulation with the data.

The mechanical design allows for the versatile combination of individual detectors for various experimental purposes. The two XtRa detectors were coupled with a silicon cube in the ^{22}Al and ^{26}P β decay experiment [76] and coupled with a Time Projection Chamber in the ^{220}Rn α decay experiment [77]. We also have the option to integrate LEGe and the central chamber with larger Germanium detector arrays, such as the DEcay Germanium Array initiator [78], to achieve a higher γ-ray detection efficiency.

5.3. α-particle measurements

Figure 10 shows the α spectrum measured by MSD26 using an ^{241}Am source, with a 2-mm diameter aperture installed in front. Figure 11 shows the ΔE-E α spectra measured by the telescope formed by MSD12 and MSD26. The α sum peak exhibits an energy resolution of 0.95%. We first installed MSD26 and calibrated it using ^{148}Gd ($E_\alpha = 3182.68$ keV [79]) and ^{241}Am sources, and then measured the residual energy of ^{241}Am α particles in MSD26 with MSD12 installed in front of it. This allowed us to accurately determine the effective thickness of MSD12 to be 11.65(8) μm, taking into account the thickness of 0.35 μm of the 9.5P/7P window. The total thickness of MSD12 is in agreement with the nominal value of 12 μm given in the Micron datasheet.

5.4. Coincidence measurements

We placed an ^{241}Am source at the center of the chamber, 11.7 mm away from MSD12 and 10.5 mm away from the entrance window of LEGe. Figure 12 shows the α-γ coincidence spectrum between the MSD detector telescope and LEGe. The majority of low-energy photons emitted from ^{241}Am are blocked by the source substrate, leaving only the 59.5-keV γ ray in ^{237}Np and its escape peaks noticeable.

We placed an ^{152}Eu source at the center of the chamber. Figure 13 shows the XtRa1 γ spectra gated by the Sm K X rays measured by LEGe and gated by the electrons measured by MSD26, respectively. By applying the characteristic X-ray coincidence condition, both the room background γ rays and the β^--delayed ^{152}Gd γ rays are substantially suppressed. Conversely, the electron coincidence condition suppresses the room background and the EC-delayed ^{152}Sm γ rays. Having the ability to detect electrons and positrons would help clean up the in-beam spectrum, thereby facilitating the identification of γ ray origins.

5.5. Timing performance

The timing performance of electronics was first tested using a Canberra Model 1407P Pulse Pair Generator [81]. The dual pulses were separately fed into two Pixie-16 channels. The FWHM resolution of the time-difference distribution is estimated to be 0.46 ns. Then, the primary pulse was split and fed to each test input of preamplifiers, and the resulting FWHM timing resolutions are 37.4 ns (MSD12), 4.4 ns (MSD26), 1.2 ns (XtRa1), 1.8 ns (XtRa2). The amplitude resolutions obtained from the pulse test are 0.13% (Pulser), 3.17% (MSD12), 0.84% (MSD26), 0.26% (XtRa1), and 0.24% (XtRa2), demonstrating the electronics noise level present in the system.

The timing performance of the detectors was studied using an ^{241}Am source placed inside the chamber and a ^{152}Eu source placed outside of the chamber. The sources were positioned in such a way that the α-γ coincidences could be measured by MSD and LEGe, and γ-γ coincidences could be measured by LEGe and XtRa. Fig. 14 shows the time difference distributions between all the coincidences without any energy restrictions. Based on these measurements, an event-build window can be defined to capture all prompt coincidences and some chance continuum for background subtraction in offline analysis. Note that the asymmetric tail in both α-γ time difference distributions is attributed to the relatively long-lived 59.5-keV excited state of ^{237}Np.

Figure 15 shows the α-γ time difference distribution constructed by the start timestamps from 5486-keV α measured by the two MSDs and the stop timestamps from the 59.5-keV γ ray deexciting the 59.5-keV state in ^{237}Np measured by LEGe. By fitting the time spectra with a function

$$f(t; N, T_{1/2}, B) = \frac{N \ln(2)}{T_{1/2}} \exp\left[-\frac{t \ln(2)}{T_{1/2}}\right] + B \qquad (5)$$

composed of the total number of decays (N), the exponential decay half-life ($T_{1/2}$), and a constant background (B), we
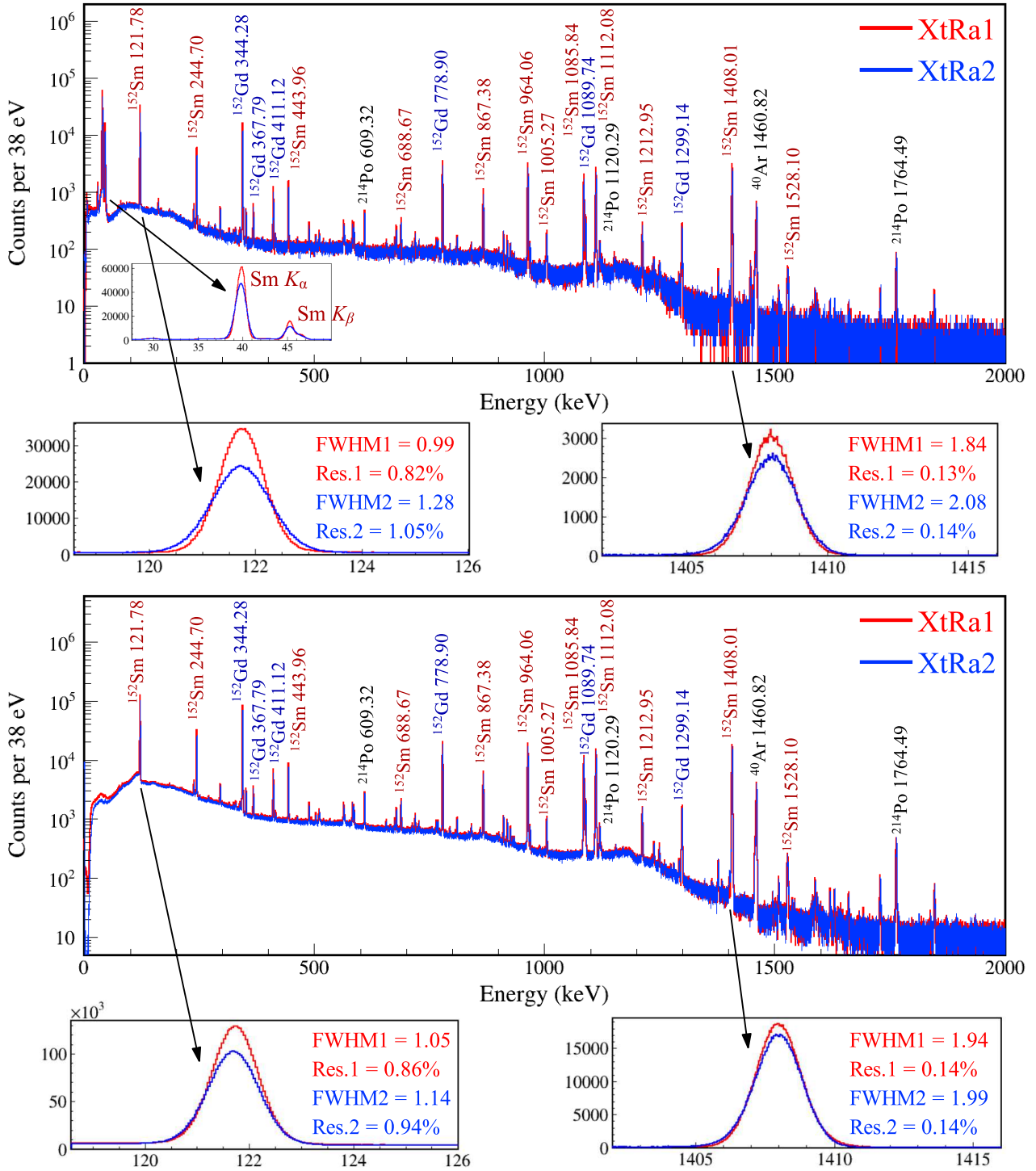
Figure 8: γ-ray spectra measured by XtRa1 (red) and XtRa2 (blue) using an ^{152}Eu source. Upper panel: the ^{152}Eu source is placed in the middle of the two XtRa facing each other. Lower panel: the ^{152}Eu source is placed at the center of the vacuum chamber, with the two XtRa detectors positioned according to the configuration shown in Fig. 4. All the γ-ray energy values are adopted from Ref. [71] rounded to the nearest 0.01 keV. The insets demonstrate the detector responses at 122 and 1408 keV.
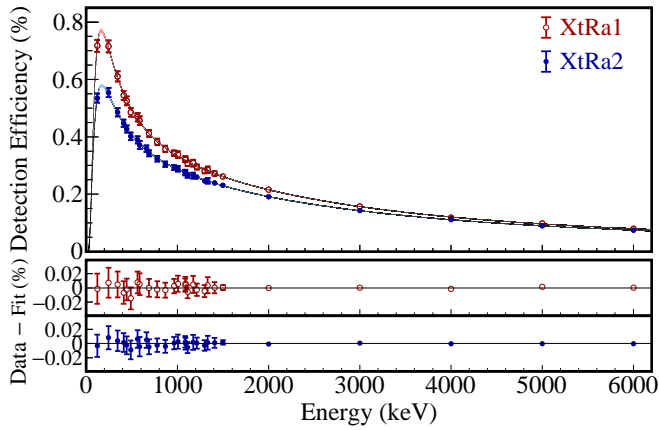
Figure 9: Absolute γ-ray detection efficiency of the two XtRa detectors obtained using ^{152}Eu, ^{137}Cs, and ^{60}Co sources placed at the center of the chamber. The ^{137}Cs data point at 662 keV is only applicable to XtRa2 due to the source placement. The 6 data points above 1500 keV are GEANT4 simulated efficiencies scaled by a factor to match the low-energy source data. The efficiency curves along with the 1σ uncertainty bands are generated by fitting all data points.
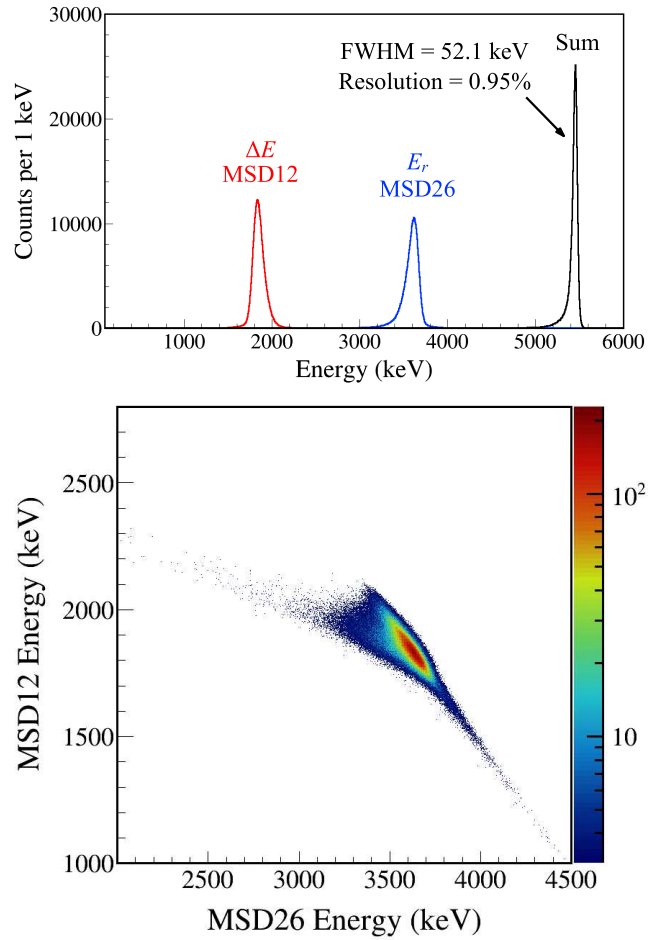
Figure 11: Upper: α-energy spectra measured by MSD12 (red), MSD26 (blue), and MSD12+MSD26 (black) using an ^{241}Am source. Lower: ΔE-E 2D plot.
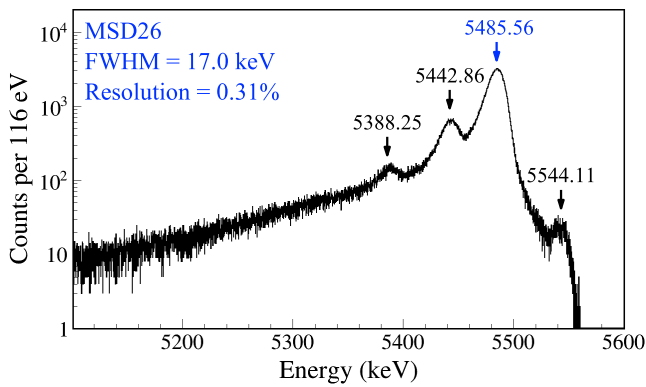
Figure 10: α spectrum measured by MSD26 using an ^{241}Am source. The α energy values are adopted from Ref. [80] rounded to the nearest 0.01 keV.
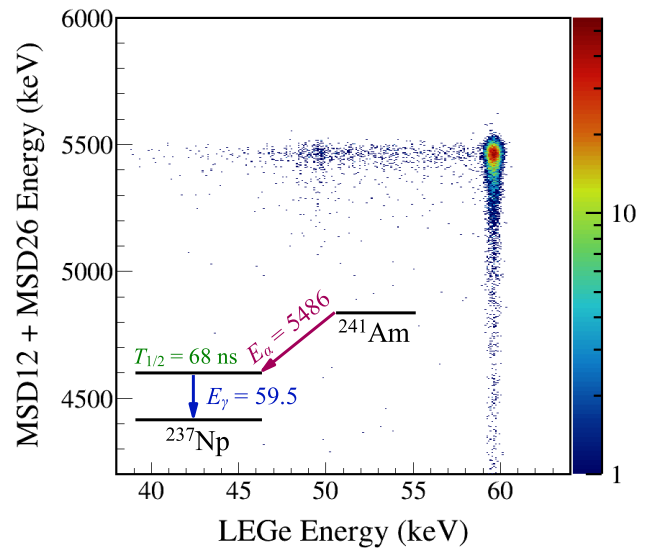

Figure 12: Coincidence spectrum between the MSD detector telescope and LEGe obtained using an ^{241}Am source placed at the center of the chamber. A simplified ^{241}Am decay scheme shows the dominant α-γ sequence.
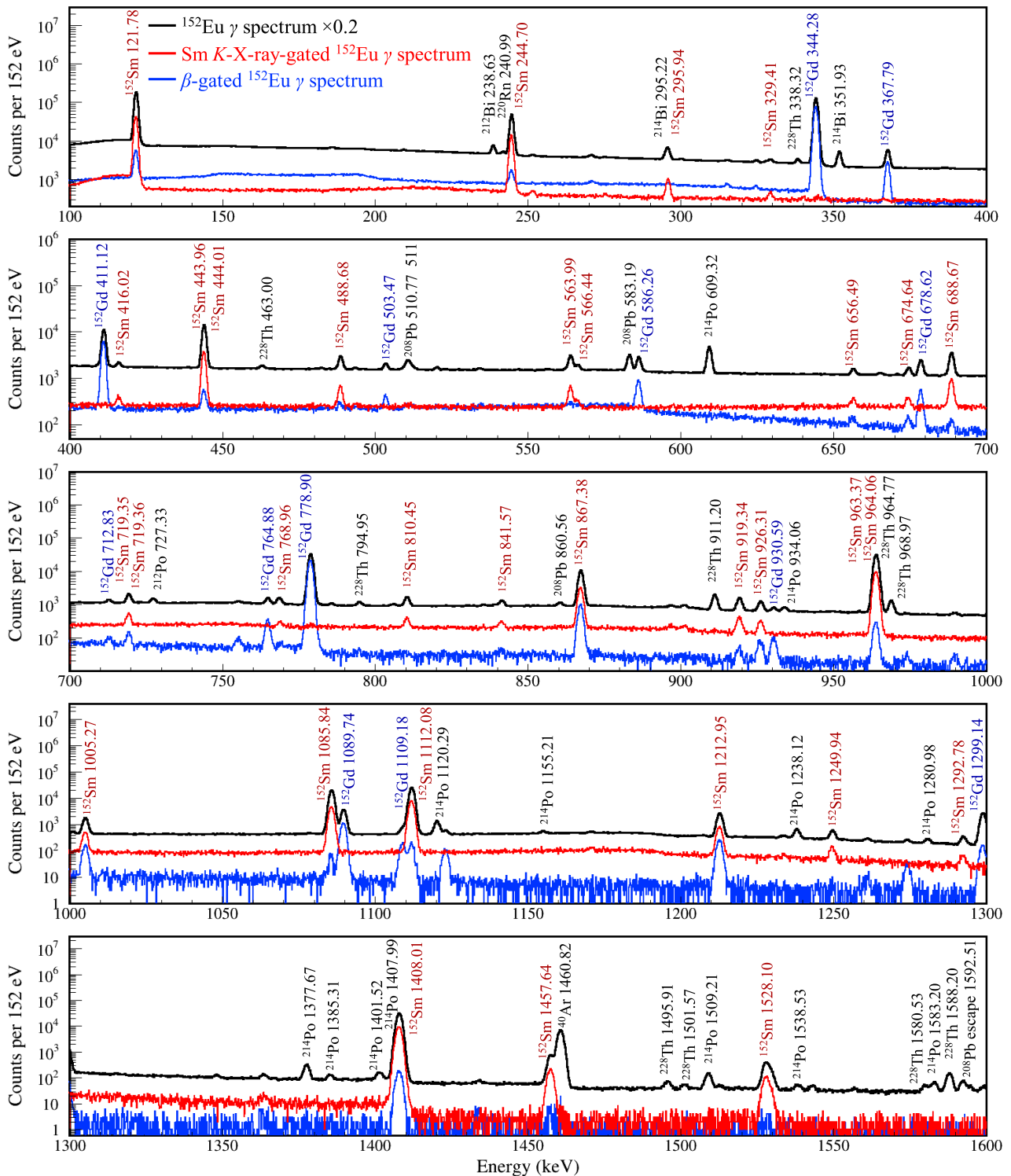
Figure 13: Black represents the raw γ-ray spectrum measured by XtRa1 using an ^{152}Eu source placed at the center of the chamber. Red represents the XtRa1 γ-ray spectrum gated by the Sm K_α and K_β X rays measured by LEGe. Blue represents the XtRa1 γ-ray spectrum gated by the electrons measured by MSD26. The raw spectrum is scaled down by a factor of 5 for better comparison.

14

obtained the half-life of the 59.5-keV excited state in ^{237}Np to be 68.4(9) ns (MSD12) and 68.0(6) ns (MSD26), respectively. Two factors may limit the time resolution that can be achieved with semiconductor detectors. Firstly, the charge collection process is inherently slow, typically taking several hundred nanoseconds. This timescale is much longer than the output from scintillators, making it hard to achieve the same level of timing performance. Secondly, the pulse rise shape from semiconductor detectors can vary significantly from event to event, resulting in a larger uncertainty in generating timestamps. Nevertheless, the results obtained from both Si detectors are consistent with recent precision measurements of 67.86(9) ns [83] and 67.60(25) ns [84], thereby providing validation for the PXCT electronics configurations.
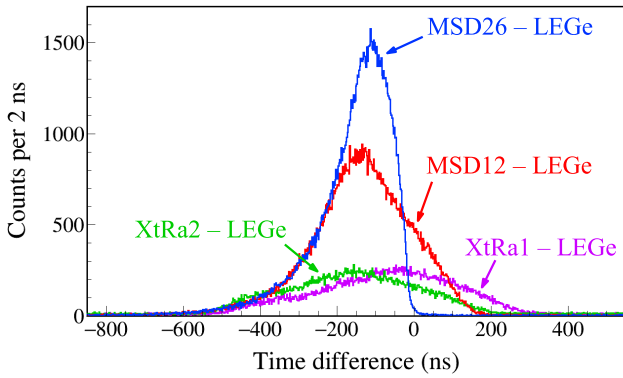

Figure 14: Coincidence time spectra between each detector obtained using an ^{241}Am source placed at the center of the chamber and a ^{152}Eu source placed outside of the chamber. The timestamps of the LEGe signals serve as the common reference for the other four detectors.
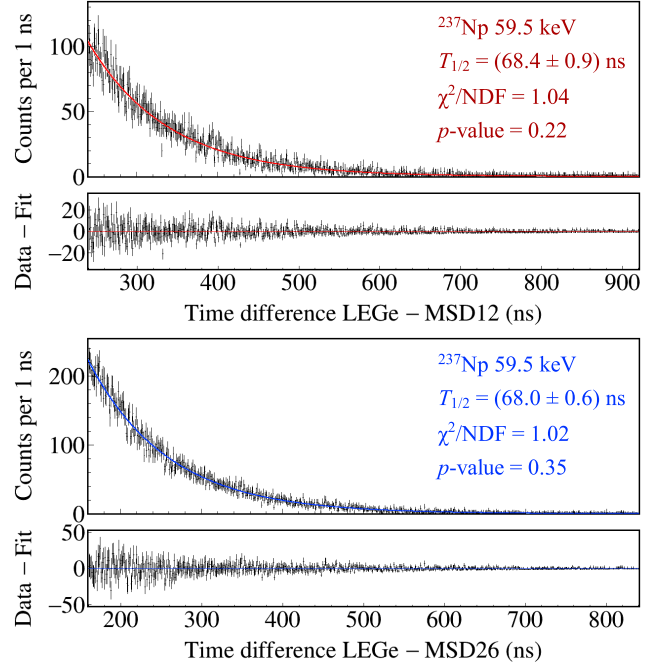

Figure 15: Time differences between the 59.5-keV γ-ray signals in LEGe and the 5486-keV α signals in the MSD silicon detector telescope.

6. Summary & Outlook

The design, construction, and radioactive source test results of the PXCT detection system are reported. This setup has the ability to detect all particles emitted in the EC/β^+ decay of ^{60}Ga, enabling us to determine the lifetimes, the proton, α, and γ-ray branching ratios for discrete ^{60}Zn resonances for the first time. This setup can also provide experimental information on the nuclear level density and transmission coefficients needed to calculate rates using the statistical model. A comprehensive dataset on ^{60}Zn resonances would offer valuable insights into the competition between the ^{59}Cu$(p, \gamma)^{60}$Zn and ^{59}Cu$(p, \alpha)^{56}$Ni reactions and allow for more accurate modeling of X-ray burst observables.

The PXCT approach has applicability to constrain other key reaction rates in the rp-process. For instance, ^{64}Ge plays an analogous role in the ZnGa cycle (Fig. 2) to the role of ^{60}Zn in the NiCu cycle [17]. Given the similarity of the Q_{EC}, half-lives, proton/α-separation energies, and X-ray energies, it is technically possible to extend this method to study the β-decay of ^{64}As in the future.

References

[1] J. C. Hardy, J. A. Macdonald, H. Schmeing, H. R. Andrews, J. S. Geiger, R. L. Graham, T. Faestermann, E. T. H. Clifford, and K. P. Jackson, Phys. Rev. Lett. 37, 133 (1976).

[2] J. H. Scofield, *Atomic Inner-Shell Processes* (Academic Press: New York (NY), USA, 1975).

[3] W. Bambynek, B. Crasemann, R. W. Fink, H. U. Freund, H. Mark, C. D. Swift, R. E. Price, and P. Venugopala Rao, Rev. Mod. Phys. 44, 716 (1972).

[4] J. Giovinazzo, Ph. Dessagne, and Ch. Miehé, Nucl. Phys. A 674, 394 (2000).

[5] J. A. Macdonald, J. C. Hardy, H. Schmeing, T. Faestermann, H. R. Andrews, J. S. Geiger, R. L. Graham, and K. P. Jackson, Nucl. Phys. A 288, 1 (1977).

[6] P. Asboe-Hansen, E. Hagberg, P. G. Hansen, J. C. Hardy, P. Hornshøj, B. Jonson, S. Mattsson, P. Tidemand-Petersson, Phys. Lett. B 77, 363 (1978).

[7] P. Asboe-Hansen, E. Hagberg, P. G. Hansen, J. C. Hardy, B. Jonson, and S. Mattsson, Nucl. Phys. A 361, 23 (1981).

[8] Z. Janas, L. Batist, R. Borcea, J. Döring, M. Gierlik, M. Karny, R. Kirchner, M. La Commara, S. Mandal, C. Mazzocchi, F. Moroz, S. Orlov, A. Płochocki, E. Roeckl, and J. Żylicz, Eur. Phys. J. A 24, 205 (2005).

[9] Z. Janas, L. Batist, J. Döring, M. Gierlik, R. Kirchner, J. Kurcewicz, H. Mahmud, C. Mazzocchi, A. Płochocki, E. Roeckl, K. Schmidt, P. J. Woods, and J. Żylicz, Eur. Phys. J. A 23, 401 (2005).

[10] J. José, *Stellar Explosions: Hydrodynamics and Nucleosynthesis* (CRC/Taylor and Francis: Boca Raton (FL), USA, 2016).

[11] H. Schatz and K. E. Rehm, Nucl. Phys. A 777, 601 (2006).

[12] A. Parikh, J. José, G. Sala, and C. Iliadis, Prog. Part. Nucl. Phys. 69, 225 (2013).

[13] L. van Wormer, J. Görres, C. Iliadis, M. Wiescher, and F.-K. Thielemann, Astrophys. J. 432, 326 (1994).

[14] Richard H. Cyburt, A. Matthew Amthor, Ryan Ferguson, Zach Meisel, Karl Smith, Scott Warren, Alexander Heger, R. D. Hoffman, Thomas Rauscher, Alexander Sakharuk, Hendrik Schatz, F. K. Thielemann, Michael Wiescher, Astrophys. J. Suppl. Ser. 189, 240 (2010).

[15] T. Rauscher and F. K. Thielemann, At. Data Nucl. Data Tables 75, 1 (2000).

[16] A. Parikh, J. José, F. Moreno, and C. Iliadis, Astrophys. J. Suppl. Ser. 178, 110 (2008).

[17] R. H. Cyburt, A. M. Amthor, A. Heger, E. Johnson, L. Keek, Z. Meisel, H. Schatz, and K. Smith, Astrophys. J. 830, 55 (2016).

[18] Zach Meisel, Grant Merz, and Sophia Medvid, Astrophys. J. 872, 84 (2019).

[19] C. Fröhlich, G. Martínez-Pinedo, M. Liebendörfer, F.-K. Thielemann, E. Bravo, W. R. Hix, K. Langanke, and N. T. Zinner, Phys. Rev. Lett. 96, 142502 (2006).

[20] A. Arcones, C. Fröhlich, and G. Martínez-Pinedo, Astrophys. J. 750, 18 (2012).

[21] C. E. Rolfs and W. S. Rodney, *Cauldrons in the Cosmos* (University of Chicago, Chicago, 1988).

[22] D. Soltesz, M. A. A. Mamun, A. V. Voinov, Z. Meisel, B. A. Brown, C. R. Brune, S. M. Grimes, H. Hadizadeh, M. Hornish, T. N. Massey, J. E. O'Donnell, and W. E. Ormand, Phys. Rev. C 103, 015802 (2021).

[23] C. Iliadis, *Nuclear Physics of Stars* (Wiley-VCH, Verlag, Wenheim, Germany, 2015).

[24] J. S. Randhawa, R. Kanungo, J. Refsgaard, P. Mohr, T. Ahn, M. Alcorta, C. Andreoiu, S. S. Bhattacharjee, B. Davids, G. Christian, A. A. Chen, R. Coleman, P. E. Garrett, G. F. Grinyer, E. Gyabeng Fuakye, G. Hackman, J. Hollett, R. Jain, K. Kapoor, R. Krücken, A. Laffoley, A. Lennarz, J. Liang, Z. Meisel, B. Nikhil, A. Psaltis, A. Radich, M. Rocchini, N. Saei, M. Saxena, M. Singh, C. Svensson, P. Subramaniam, A. Talebitaher, S. Upadhyayula, C. Waterfield, J. Williams, and M. Williams, Phys. Rev. C 104, L042801 (2022).

[25] Chanhee Kim, Kyungyuk Chae, Soomi Cha, Kyujin Kwak, Gwangeon Seong, and Michael Smith, Astrophys. J. 929, 96 (2022).

[26] Connor O'Shea, unpublished.

[27] Gerard Owens-Fryar, unpublished.

[28] M. Wang, W. J. Huang, F. G. Kondev, G. Audi, S. Naimi, Chin. Phys. C 45, 030003 (2021).

[29] S. E. A. Orrigo, B. Rubio, W. Gelletly, P. Aguilera, A. Algora, A. I. Morales, J. Agramunt, D. S. Ahn, P. Ascher, B. Blank, C. Borcea, A. Boso, R. B. Cakirli, J. Chiba, G. de Angelis, G. de France, F. Diel, P. Doornenbal, Y. Fujita, N. Fukuda, E. Ganioğlu, M. Gerbaux, J. Giovinazzo, S. Go, T. Goigoux, S. Grévy, V. Guadilla, N. Inabe, G. G. Kiss, T. Kubo, S. Kubono, T. Kurtukian-Nieto, D. Lubos, C. Magron, F. Molina, A. Montaner-Pizá, D. Napoli, D. Nishimura, S. Nishimura, H. Oikawa, V. H. Phong, H. Sakurai, Y. Shimizu, C. Sidong, P.-A. Söderström, T. Sumikama, H. Suzuki, H. Takeda, Y. Takei, M. Tanaka, J. Wu, and S. Yagi, Phys. Rev. C 103, 014324 (2021).

[30] S. F. Paul, J. Bergmann, J. D. Cardona, K. A. Dietrich, E. Dunling, Z. Hockenbery, C. Hornung, C. Izzo, A. Jacobs, A. Javaji, B. Kootte, Y. Lan, E. Leistenschneider, E. M. Lykiardopoulou, I. Mukul, T. Murböck, W. S. Porter, R. Silwal, M. B. Smith, J. Ringuette, T. Brunner, T. Dickel, I. Dillmann, G. Gwinner, M. MacCormick, M. P. Reiter, H. Schatz, N. A. Smirnova, J. Dilling, and A. A. Kwiatkowski, Phys. Rev. C 104, 065803 (2021).

[31] T. Rauscher, Phys. Rev. C 81, 045807 (2010).

[32] Huo Junde, Huo Su, Yang Dong, Nucl. Data Sheets 112, 1513 (2011).

[33] M. Shamsuzzoha Basunia, Nucl. Data Sheets 151, 1 (2018).

[34] E. Browne and J. K. Tuli, Nucl. Data Sheets 114, 1849 (2013).

[35] C. Mazzocchi, Z. Janas, J. Döring, M. Axiotis, L. Batist, R. Borcea, D. Cano-Ott, E. Caurier, G. de Angelis, E. Farnea, A. Faßbender, A. Gadea, H. Grawe, A. Jungclaus, M. Kapica, R. Kirchner, J. Kurcewicz, S.M. Lenzi, T. Martínez, I. Mukha, E. Nácher, D. R. Napoli, E. Roeckl, B. Rubio, R. Schwengner, J. L. Tain, and C. A. Ur, Eur. Phys. J. A 12, 269 (2001).

[36] M. J. López Jiménez, B. Blank, M. Chartier, S. Czajkowski, P. Dessagne, G. de France, J. Giovinazzo, D. Karamanis, M. Lewitowicz, V. Maslov, C. Miehé, P. H. Regan, M. Stanoiu, and M. Wiescher, Phys. Rev. C 66, 025803 (2002).

[37] L. Kucuk, S. E. A. Orrigo, A. Montaner-Pizá, B. Rubio, Y. Fujita, W. Gelletly, B. Blank, Y. Oktem, T. Adachi, A. Algora, P. Ascher, R. B. Cakirli, G. de France, H. Fujita, E. Ganioğlu, J. Giovinazzo, S. Grévy, F. M. Marqués, F. Molina, F. de Oliveira Santos, L. Perrot, R. Raabe, P. C. Srivastava, G. Susoy, A. Tamii, J. C Thomas, Eur. Phys. J. A 53, 134 (2017).

[38] R. Kamermans, H. W. Jongsma, J. van der Spek, and H. Verheul, Phys. Rev. C 10, 620 (1974).

[39] Carl Svensson, Ph.D. Thesis, McMaster University, Ontario, Canada, 1998.

[40] Gamma to Level Scheme Computation.

[41] M. Honma, T. Otsuka, B. A. Brown, and T. Mizusaki, Phys. Rev. C 69, 034335 (2004).

[42] B. A. Brown and W. D. M. Rae, Nucl. Data Sheets 120, 115 (2014).

[43] Radiation Report.

[44] J. Wei, H. Ao, B. Arend, S. Beher, G. Bollen, N. Bultman, F. Casagrande, W. Chang, Y. Choi, S. Cogan, C. Compton, M. Cortesi, J. Curtin, K. Davidson, X. Du, K. Elliott, B. Ewert, A. Facco, A. Fila, K. Fukushima, V. Ganni, A. Ganshyn, J. Gao, T. Glasmacher, J. Guo, Y. Hao, W. Hartung, N. Hasan, M. Hausmann, K. Holland, H. C. Hseuh, M. Ikegami, D. Jager, S. Jones, N. Joseph, T. Kanemura, S.-H. Kim, P. Knudsen, B. Kortum, E. Kwan, T. Larter, R. E. Laxdal, M. Larmann, K. Laturkar, J. LeTourneau, Z.-Y. Li, S. Lidia, G. Machicoane, C. Magsig, P. Manwiller, F. Marti, T. Maruta, A. McCartney, E. Metzgar, S. Miller, Y. Momozaki, D. Morris, M. Mugerian, I. Nesterenko, C. Nguyen, W. O'Brien, K. Openlander, P. N. Ostroumov, M. Patil, A. S. Plastun, J. Popielarski, L. Popielarski, M. Portillo, J. Priller, X. Rao, M. Reaume, H. Ren, K. Saito, M. Smith, M. Steiner, A. Stolz, O. B. Tarasov, B. Tousignant, R. Walker, X. Wang, J. Wenstrom, G. West, K. Witgen, M. Wright, T. Xu, Y. Xu, Y. Yamazaki, T. Zhang, Q. Zhao, S. Zhao, K. Dixon, M. Wiseman, M. Kelly, K. Hosoyama, and S. Prestemon, Mod. Phys. Lett. A 37, 2230006 (2022).

[45] M. Portillo, B.M. Sherrill, Y. Choi, M. Cortesi, K. Fukushima, M. Hausmann, E. Kwan, S. Lidia, P.N. Ostroumov, R. Ringle, M.K. Smith, M. Steiner, O.B. Tarasov, A.C.C. Villari, and T. Zhang, Nucl. Instrum. Methods Phys. Res. B 540, 151 (2023).

[46] C.S. Sumithrarachchi, D.J. Morrissey, S. Schwarz, K. Lund, G. Bollen, R. Ringle, G. Savard, and A.C.C. Villari, Nucl. Instrum. Methods Phys. Res. B 463, 305 (2020).

[47] K.R. Lund, G. Bollen, D. Lawton, D.J. Morrissey, J. Ottarson, R.

Ringle, S. Schwarz, C.S. Sumithrarachchi, A.C.C. Villari, and J. Yurkon, Nucl. Instrum. Methods Phys. Res. B **463**, 378 (2020).

[48] A.C.C. Villari, G. Bollen, A. Henriques, A. Lapierre, S. Nash, R. Ringle, S. Schwarz, C.S. Sumithrarachchi, Nucl. Instrum. Methods Phys. Res. B **541**, 350 (2023).

[49] MIRCON MSD12 Circular Silicon Detector.

[50] MIRCON MSD26 Circular Silicon Detector.

[51] MIRION Low Energy Germanium Detector.

[52] MIRION Extended Range Coaxial Germanium Detector.

[53] MIRION Cryo-Pulse 5 PLUS Electrically Refrigerated Cryostat.

[54] D. Willems, R. Arts, B.V.-J. Douwen, MIRION Technical Paper (2015).

[55] MIRION Intelligent Preamplifier.

[56] ORTEC 660 Dual 5-kV Bias Supply.

[57] Mesytec MPR-1 Charge Integrating Preamplifier.

[58] Mesytec MHV-4 High Voltage Supply.

[59] Mesytec MNV-4 NIM Power Supply.

[60] XIA Pixie-16 Digitizer.

[61] K. Starosta, C. Vaman, D. Miller, P. Voss, D. Bazin, T. Glasmacher, H. Crawford, P. Mantica, H. Tan, W. Hennig, M. Walby, A. Fallu-Labruyere, J. Harris, D. Breus, P. Grudberg, W.K. Warburton, Nucl. Instrum. Methods Phys. Res. A **610**, 700 (2009).

[62] C.J. Prokop, S.N. Liddick, B.L. Abromeit, A.T. Chemey, N.R. Larson, S. Suchyta, J.R. Tompkins, Nucl. Instrum. Methods Phys. Res. A **741**, 163 (2014).

[63] XIA Pixie-16 Digitizer User Manual.

[64] H.Y. Wu, Z.H. Li, H. Tan, H. Hua, J. Li, W. Hennig, W.K. Warburton, D.W. Luo, X. Wang, X.Q. Li, S.Q. Zhang, C. Xu, Z.Q. Chen, C.G. Wu, Y. Jin, J. Lin, D.X. Jiang, Y.L. Ye, Nucl. Instrum. Methods Phys. Res. A **975**, 164200 (2020).

[65] BNC Model DB-2 NIM Random Pulse Generator.

[66] B. E. Glassman, D. Pérez-Loureiro, C. Wrede, J. Allen, D. W. Bardayan, M. B. Bennett, K. A. Chipps, M. Febbraro, M. Friedman, C. Fry, M. R. Hall, O. Hall, S. N. Liddick, P. O'Malley, W. -J. Ong, S. D. Pain, S. B. Schwartz, P. Shidling, H. Sims, L. J. Sun, P. Thompson, and H. Zhang, Phys. Rev. C **99**, 065801 (2019).

[67] L. J. Sun, M. Friedman, T. Budner, D. Pérez-Loureiro, E. Pollacco, C. Wrede, B. A. Brown, M. Cortesi, C. Fry, B. E. Glassman, J. Heideman, M. Janasik, A. Kruskie, A. Magilligan, M. Roosa, J. Stomps, J. Surbrook, and P. Tiwari, Phys. Rev. C **103**, 014322 (2021).

[68] Matt Newville, easyXAFS, Matteo Levantino, Christian Schlepuetz, Damian Günzing, Max Rakitin, Sang-Woo Kim, and kalvdans, xraypy/XrayDB: (4.5.1). Zenodo (2023).

[69] M.-M. Bé, V. Chisté, C. Dulieu, X. Mougeot, E. Browne, V. Chechev, N. Kuzmenko, F. Kondev, A. Luca, M. Galán, A.L. Nichols, A. Arinc, and X. Huang, Table of Radionuclides, Bureau International des Poids et Mesures (2004).

[70] M. Basunia, Nucl. Data Sheets **107**, 2323 (2006).

[71] M. J. Martin, Nucl. Data Sheets **114**, 1497 (2013).

[72] D. Weisshaar, D. Bazin, P.C. Bender, C.M. Campbell, F. Recchia, V. Bader, T. Baugher, J. Belarge, M.P. Carpenter, H.L. Crawford, M. Cromaz, B. Elman, P. Fallon, A. Forney, A. Gade, J. Harker, N. Kobayashi, C. Langer, T. Lauritsen, I.Y. Lee, A. Lemasson, B. Longfellow, E. Lunderberg, A.O. Macchiavelli, K. Miki, S. Momiyama, S. Noji, D.C. Radford, M. Scott, J. Sethi, S.R. Stroberg, C. Sullivan, R. Titus, A. Wiens, S. Williams, K. Wimmer, S. Zhu, Nucl. Instrum. Methods Phys. Res. A **847**, 187 (2017).

[73] M. B. Bennett, C. Wrede, S. N. Liddick, D. Pérez-Loureiro, D. W. Bardayan, B. A. Brown, A. A. Chen, K. A. Chipps, C. Fry, B. E. Glassman, C. Langer, N. R. Larson, E. I. McNeice, Z. Meisel, W. Ong, P. D. O'Malley, S. D. Pain, C. J. Prokop, H. Schatz, S. B. Schwartz, S. Suchyta, P. Thompson, M. Walters, and X. Xu, Phys. Rev. C **97**, 065803 (2018).

[74] S. Agostinelli, J. Allison, K. Amako, J. Apostolakis, H. Araujo, P. Arce, M. Asai, D. Axen, S. Banerjee, G. Barrand, F. Behner, L. Bellagamba, J. Boudreau, L. Broglia, A. Brunengo, H. Burkhardt, S. Chauvie, J. Chuma, R. Chytracek, G. Cooperman, G. Cosmo, P. Degtyarenko, A. Dell'Acqua, G. Depaola, D. Dietrich, R. Enami, A. Feliciello, C. Ferguson, H. Fesefeldt, G. Folger, F. Foppiano, A. Forti, S. Garelli, S. Giani, R. Giannitrapani, D. Gibin, J. J. Gómez Cadenas, I. González, G. Gracia Abril, G. Greeniaus, W. Greiner, V. Grichine, A. Grossheim, S. Guatelli, P. Gumplinger, R. Hamatsu, K. Hashimoto, H. Hasui, A.

Heikkinen, A. Howard, V. Ivanchenko, A. Johnson, F. W. Jones, J. Kallenbach, N. Kanaya, M. Kawabata, Y. Kawabata, M. Kawaguti, S. Kelner, P. Kent, A. Kimura, T. Kodama, R. Kokoulin, M. Kossov, H. Kurashige, E. Lamanna, T. Lampén, V. Lara, V. Lefebure, F. Lei, M. Liendl, W. Lockman, F. Longo, S. Magni, M. Maire, E. Medernach, K. Minamimoto, P. Mora de Freitas, Y. Morita, K. Murakami, M. Nagamatu, R. Nartallo, P. Nieminen, T. Nishimura, K. Ohtsubo, M. Okamura, S. O'Neale, Y. Oohata, K. Paech, J. Perl, A. Pfeiffer, M. G. Pia, F. Ranjard, A. Rybin, S. Sadilov, E. Di Salvo, G. Santin, T. Sasaki, N. Savvas, Y. Sawada, S. Scherer, S. Sei, V. Sirotenko, D. Smith, N. Starkov, H. Stoecker, J. Sulkimo, M. Takahata, S. Tanaka, E. Tcherniaev, E. Safai Tehrani, M. Tropeano, P. Truscott, H. Uno, L. Urban, P. Urban, M. Verderi, A. Walkden, W. Wander, H. Weber, J. P. Wellisch, T. Wenaus, D. C. Williams, D. Wright, T. Yamada, H. Yoshida, and D. Zschiesche, Nucl. Instrum. Methods Phys. Res. A **506**, 250 (2003).

[75] J. Allison, K. Amako, J. Apostolakis, P. Arce, M. Asai, T. Aso, E. Bagli, A. Bagulya, S. Banerjee, G. Barrand, B.R. Beck, A.G. Bogdanov, D. Brandt, J.M.C. Brown, H. Burkhardt, Ph. Canal, D. Cano-Ott, S. Chauvie, K. Cho, G.A.P. Cirrone, G. Cooperman, M.A. Cortés-Giraldo, G. Cosmo, G. Cuttone, G. Depaola, L. Desorgher, X. Dong, A. Dotti, V.D. Elvira, G. Folger, Z. Francis, A. Galoyan, L. Garnier, M. Gayer, K.L. Genser, V.M. Grichine, S. Guatelli, P. Guèye, P. Gumplinger, A.S. Howard, I. Hřivnáčová, S. Hwang, S. Incerti, A. Ivanchenko, V.N. Ivanchenko, F.W. Jones, S.Y. Jun, P. Kaitaniemi, N. Karakatsanis, M. Karamitros, M. Kelsey, A. Kimura, T. Koi, H. Kurashige, A. Lechner, S.B. Lee, F. Longo, M. Maire, D. Mancusi, A. Mantero, E. Mendoza, B. Morgan, K. Murakami, T. Nikitina, L. Pandola, P. Paprocki, J. Perl, I. Petrović, M.G. Pia, W. Pokorski, J.M. Quesada, M. Raine, M.A. Reis, A. Ribon, A. Ristić Fira, F. Romano, G. Russo, G. Santin, T. Sasaki, D. Sawkey, J.I. Shin, I.I. Strakovsky, A. Taborda, S. Tanaka, B. Tomé, T. Toshito, H.N. Tran, P.R. Truscott, L. Urban, V. Uzhinsky, J.M. Verbeke, M. Verderi, B.L. Wendt, H. Wenzel, D.H. Wright, D.M. Wright, T. Yamashita, J. Yarba, H. Yoshida, Nucl. Instrum. Methods Phys. Res. A **835**, 186 (2016).

[76] Erik Jensen, Ph.D. Thesis, Aarhus University, Aarhus, Denmark, 2024.

[77] R. Mahajan, T. Wheeler, E. Pollacco, C. Wrede, A. Adams, H. Alvarez-Pol, A. Andalib, A. Anthony, Y. Ayyad, D. Bazin, T. Budner, M. Cortesi, J. Dopfer, M. Friedman, A. Jaros, D. Pérez-Loureiro, B. Mehl, R. De Oliveira, L. J. Sun, and J. Surbrook, Phys. Rev. C **109**, 05xxxx (2024).

[78] FRIB Decay Station White Paper.

[79] Y.A. Akovali, Nucl. Data Sheets **84**, 1 (1998).

[80] M.-M. Bé, V. Chisté, C. Dulieu, X. Mougeot, E. Browne, V. Chechev, N. Kuzmenko, F. Kondev, A. Luca, M. Galán, A.L. Nichols, A. Arinc, and X. Huang, Table of Radionuclides, Bureau International des Poids et Mesures (2010).

[81] Canberra Model 1407P Pulse Pair Generator.

[82] D. Foreman-Mackey, D. W. Hogg, D. Lang, and J. Goodman, Publ. Astron. Soc. Pac. **125**, 306 (2013).

[83] Marcell P. Takács, Karsten Kossert, Appl. Radiat. Isot. **176**, 109858 (2021).

[84] Chavdar Dutsov, Benoît Sabot, Philippe Cassette, Krasimir Mitev, Appl. Radiat. Isot. **176**, 109845 (2021).

17